

# Nonlinear Hall Effect in Metal–Organic Frameworks

Sarbajit Mazumdar,<sup>1,\*</sup> Jagadish N S,<sup>2</sup> Awadhesh Narayan,<sup>3</sup>  
Giorgio Sangiovanni,<sup>1</sup> Ronny Thomale,<sup>1</sup> and Arka Bandyopadhyay<sup>1,†</sup>

<sup>1</sup>*Institut für Theoretische Physik und Astrophysik and Würzburg-Dresden Cluster of Excellence ctd.qmat, Universität Würzburg, Am Hubland Campus Süd, 97074 Würzburg, Germany*

<sup>2</sup>*Centre for Condensed Matter Theory, Department of Physics, Indian Institute of Science, Bengaluru, India - 560012*

<sup>3</sup>*Solid State and Structural Chemistry Unit, Indian Institute of Science, Bangalore 560012, India*  
(Dated: March 11, 2026)

We propose metal–organic frameworks (MOFs) as a versatile platform for realizing the nonlinear Hall effect. We develop an analytical down-folding scheme that maps a broad class of MOFs onto a universal effective low-energy model. As representative examples, we analyze two  $C_3$ -symmetric frameworks: Cu–dicyanoanthracene and triphenyl–metal monolayer, demonstrating how their low-energy bands can be efficiently captured by a star-lattice geometry. First-principles calculations corroborate this mapping and show that both Fermi levels lie close to symmetry-protected Dirac points. Spin–orbit coupling or inversion-symmetry breaking gaps these Dirac cones, generating Berry-curvature hotspots near the Fermi level. Supported with symmetry-based indicators, these MOFs thus suggest themselves for strain and substrate engineering as well as doping to achieve a finite nonlinear Hall response. We formulate a synthesis-oriented strategy that implements the Dirac gap directly within the framework architecture without externally applied strain. Our results establish MOFs as a broadly designable platform for engineering Berry-curvature physics and nonlinear Hall transport.

*Introduction.*— The nonlinear Hall effect (NLHE) is an unconventional transverse response that can arise in time-reversal invariant crystals when inversion symmetry is broken. In contrast to the conventional anomalous Hall effect, where the Berry curvature of Bloch bands, a geometric property that acts as an effective magnetic field in momentum space governs the linear Hall response [1–3], the NLHE originates from an asymmetric distribution of Berry curvature across the Brillouin zone [4–14]. This asymmetry, encoded in the dipolar component of the Berry curvature, provides an intrinsic mechanism for generating a second-order Hall response even in systems that preserve time-reversal symmetry. Beyond its fundamental significance, the NLHE has attracted considerable attention because higher-order transport effects offer a versatile platform for advanced functionalities, including efficient rectification [15, 16], photodetection [17], and photovoltaic responses [18]. These prospects motivate the search for material platforms in which crystal symmetry and band geometry can be engineered in a controlled manner, potentially enabling performance that surpasses conventional efficiency limits. The subtle interplay between lattice symmetry and the nonzero dipolar component makes the theoretical study of diverse lattice models both fundamental and compelling. Translating these insights into real materials with controlled symmetry modulation, however, remains a formidable experimental challenge, highlighting the gap between theory and realization. MOFs, composed of metal nodes linked by organic ligands [19, 20], form highly ordered

porous networks with exceptional structural and chemical tunability. This versatility enables precise engineering of electronic bands near the Fermi level through careful selection of metal centers and organic linkers, making MOFs an ideal platform for realizing designer lattice models with tailored symmetry and electronic properties [21]. In particular, two-dimensional (2D) MOFs have been predicted to host Dirac and flat bands, giving rise to topological insulator and Chern insulator phases [22–26]. Despite these remarkable structural and electronic features, the potential of MOFs to exhibit NLHE remains largely unexplored.

In this Letter, we address this gap by introducing a down-folding framework that maps MOFs onto effective lattice models, enabling the design of systems with strong and controllable NLHE. While this framework can be applied to a wide range of MOFs with different symmetries, our current focus is on 2D MOFs possessing  $C_3$  symmetry. We anticipate this analysis will expedite the discovery of MOFs exhibiting NLHE with other lattice symmetries as well. Specifically, we explicitly demonstrated how the experimentally relevant Cu–dicyano–anthracene (Cu–DCA) monolayer [27–29] and the triphenyl–metal (metal = Pb/Bi) MOF [22, 30] can be mapped onto an effective, down-folded star-lattice description through a real-space decimation procedure [31–34]. The renormalized hoppings for the two materials yield two distinct band topologies within the star-lattice framework, in agreement with our first-principles analysis. Notably, the Fermi level in both cases resides precisely at the Dirac point, which crucially offers the potential for Berry curvature hot spots at the Fermi surface. This mapping is not limited to these two MOFs, but can be extended to broader material classes, offering a controlled

\* sarbajit.mazumdar@uni-wuerzburg.de

† arka.bandyopadhyay@uni-wuerzburg.de

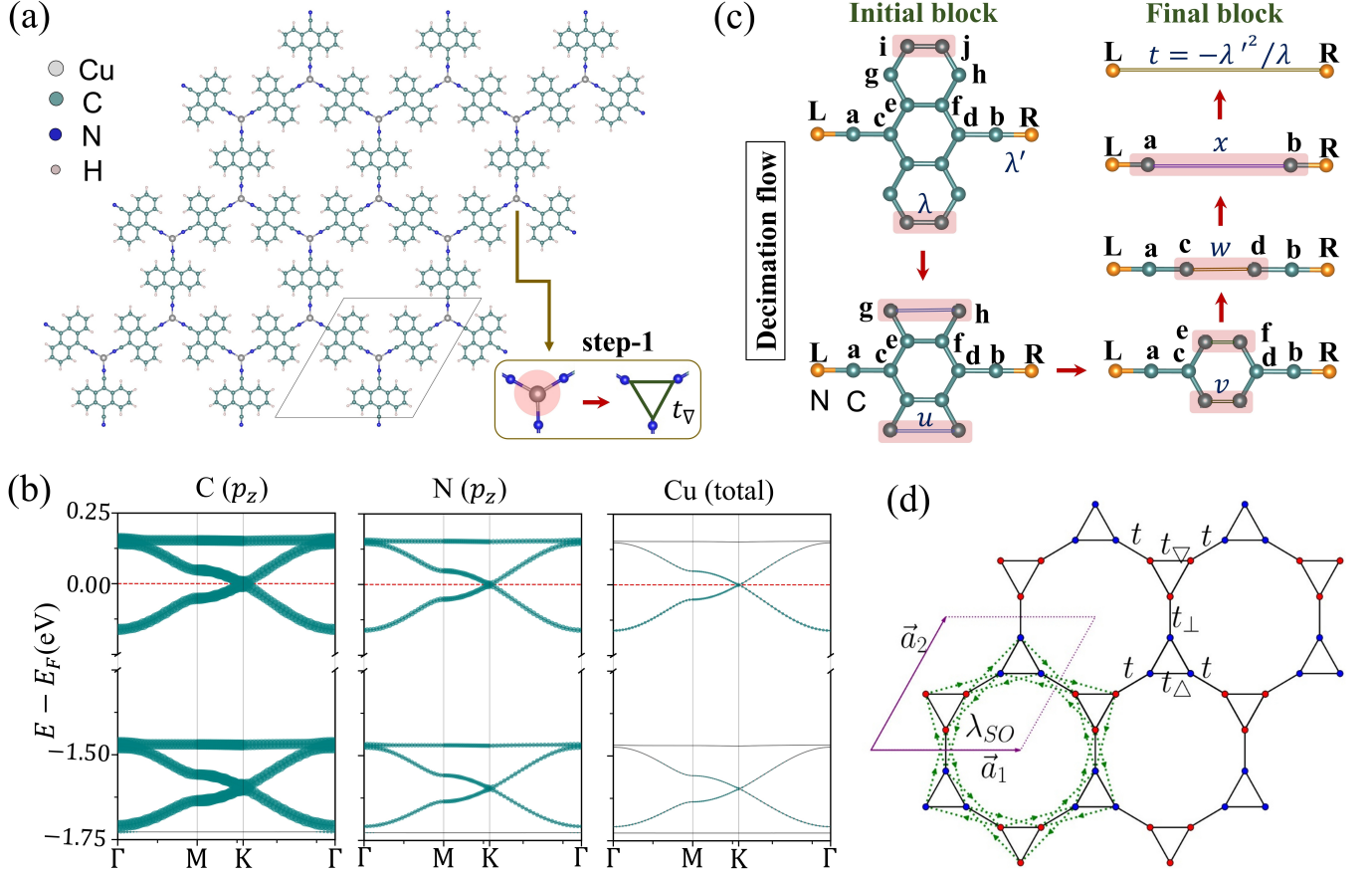


FIG. 1. **From the Cu-DCA framework to the effective star lattice.** (a) Relaxed geometry of the Cu-DCA metal-organic framework obtained from first-principles calculations. Inset: because Cu orbitals contribute negligibly near the Fermi level, the three N atoms surrounding a Cu site can be represented as an effective triangle after the first decimation step. (b) Orbital-projected band structure of Cu-DCA showing that the states near the Fermi level are predominantly derived from the  $p_z$  orbitals of C and N atoms. (c) Second decimation step for the linker segment connecting neighboring triangles. Sites removed in the downfolding are marked in red, and the renormalized hoppings between the terminal sites  $L$  and  $R$  are generated recursively. (d) Effective star lattice with a six-site unit cell spanned by lattice vectors  $\vec{a}_1$  and  $\vec{a}_2$ . Blue and red triangles carry intra-triangle hoppings  $t_{\Delta}$  and  $t_{\nabla}$ , respectively; inter-triangle bonds are described by  $t$  (and by  $t_{\perp}$  when uniaxial anisotropy is introduced). Green arrows denote the intrinsic Kane-Mele-type SOC  $\pm i\lambda_{SO}$ .

route to translate chemical and structural tunability into symmetry-selective band geometry. It enables the identification of experimentally accessible symmetry-lowering pathways, such as strain engineering and the synthesis of sister compounds that generate finite Berry curvature and an intrinsic, tunable dipolar component. This, in turn, allows for a sizable NLHE in MOFs, even without external perturbations.

*Downfolding of Cu-DCA.*— We begin with the experimentally synthesized Cu-DCA MOF, shown in Fig. 1(a) [35–39]. Its first-principles band structure [Fig. 1(b)] is semimetallic and exhibits Dirac crossings at the high-symmetry  $K$  point [27, 40]. Because gap opening at such crossings readily produces Berry-curvature hot spots, Cu-DCA is an attractive starting point for NLHE engineering once spin-orbit coupling (SOC) and inversion-symmetry breaking is introduced.

The orbital-resolved bands further show that the low-

energy states are dominated by the  $p_z$  orbitals of carbon and nitrogen, while Cu orbitals contribute only weakly in the relevant energy window [Fig. 1(b)]. This observation motivates a single-orbital description built from the C and N sites. In a first decimation step, the Cu-centered coordination environment is encoded as direct effective hopping between the three N atoms surrounding each Cu atom, so that these N sites form effective equilateral triangles [inset of Fig. 1(a)]. A second decimation step then integrates out the linker segment that connects neighboring triangles, reducing the original network to a star-lattice geometry with renormalized hopping amplitudes [Fig. 1(c)]. The analytical flow of this procedure, together with the corresponding renormalized parameters, is summarized in Supplementary Sec. S5B. The essential outcome is that Cu-DCA can be downfolded to a compact effective model that retains the Dirac crossings and low-energy band geometry relevant for the NLHE.

*Star lattice and dipolar component of Berry curvature.*— The downfolded lattice in Fig. 1(d) has a six-site unit cell composed of two inequivalent triangular motifs. We denote the intra-triangle hopping on the blue triangles by  $t_\Delta$  and that on the red triangles by  $t_\nabla$ . Neighboring blue and red triangles are connected by  $t$  in the pristine lattice and by  $(t, t_\perp)$  once uniaxial anisotropy is introduced. The effective Hamiltonian can be written as

$$\mathcal{H} = \mathcal{H}_0 + \mathcal{H}_\delta + \mathcal{H}_{\text{SO}}, \quad (1)$$

where  $\mathcal{H}_0$  contains the intra- and inter-triangle hoppings,  $\mathcal{H}_\delta$  describes inversion-symmetry-breaking onsite offsets between the two triangular subunits, and  $\mathcal{H}_{\text{SO}}$  is an intrinsic next-nearest-neighbor SOC term of Kane–Mele type. The full real-space form of these terms is given in Supplementary Sec. S1 A.

Representative band structures of the star lattice without SOC are shown in Supplementary Fig. S1.1. We focus on the parameter regime in which two kagome-like band manifolds are energetically separated, since this is the regime that reproduces the first-principles electronic structure of Cu–DCA. Once SOC and inversion-symmetry breaking are included, gaps open at the Dirac crossings. These gap openings are the source of sharply localized Berry-curvature hot spots and, once the remaining point-group symmetry is broken appropriately, of a finite dipolar component.

To make that connection explicit, we first analyze the Berry-curvature distribution of the effective model. For a two-dimensional Bloch band  $n$ , the only nonvanishing component is  $\Omega_n^z(\mathbf{k})$ , which can be written as

$$\Omega_n^z(\mathbf{k}) = -2 \text{Im} \sum_{n' \neq n} \frac{\langle u_{n\mathbf{k}} | v_x | u_{n'\mathbf{k}} \rangle \langle u_{n'\mathbf{k}} | v_y | u_{n\mathbf{k}} \rangle}{(E_n(\mathbf{k}) - E_{n'}(\mathbf{k}))^2}. \quad (2)$$

Time-reversal symmetry imposes  $\Omega_n^z(\mathbf{k}) = -\Omega_n^z(-\mathbf{k})$ , so the linear anomalous Hall response vanishes after Brillouin-zone integration. The nonlinear response, however, survives when inversion symmetry is broken because the first moment of the Berry curvature can remain finite.

Figure 2(a) shows the Berry-curvature-projected band structure for an onsite-modulated star lattice with  $\delta_1 = -0.08t$ ,  $\delta_2 = 0.08t$ , and  $t_\Delta = t_\nabla = 0.5t$ . Increasing  $\lambda_{\text{SO}}$  from  $0.04t$  to  $0.06t$  drives a clear band inversion near the  $K$  point in the positive-energy sector, accompanied by a reversal of the Berry-curvature hot spots at the avoided crossings. The associated change of topological character is confirmed by the  $\mathbb{Z}_2$  invariant obtained from the Wannier charge center (WCC) flow; see Supplementary Sec. S2 and Fig. S2.1. The same mechanism also operates in the breathing version of the star lattice, as shown in Supplementary Sec. S3.

The dipolar component tensor is defined as

$$\mathcal{D}^{ab} = \sum_n \int_{\text{BZ}} \frac{d^2k}{(2\pi)^2} f_0^{(n)}(\mathbf{k}) \partial^a \Omega_n^b(\mathbf{k}), \quad (3)$$

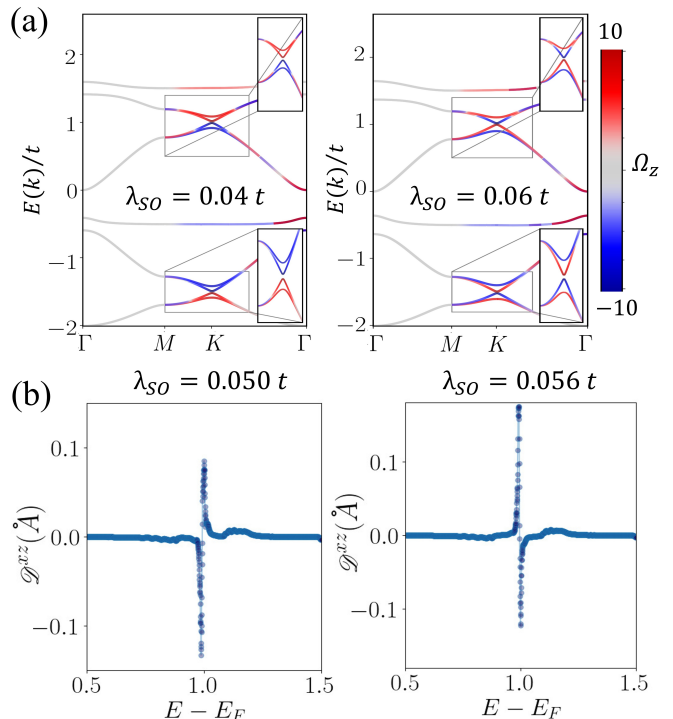


FIG. 2. **Berry curvature and its dipolar component in the star lattice.** (a) Berry-curvature-projected band structure for the onsite-modulated model with  $\delta_1 = -0.08t$ ,  $\delta_2 = 0.08t$ , and  $t_\Delta = t_\nabla = 0.5t$ , shown for two SOC strengths. Increasing  $\lambda_{\text{SO}}$  drives a band inversion near  $K$  and reverses the Berry-curvature hot spots at the avoided crossings. (b) Corresponding Berry-curvature dipole  $D^{xz}$  as a function of Fermi level for representative SOC values in the presence of a small hopping anisotropy  $t_\perp \neq t$  (here taken to model a 2% tensile strain). The strong enhancement and sign reversal near the critical point reflect the topological transition.

where  $f_0^{(n)}$  is the Fermi–Dirac distribution. Within semiclassical Boltzmann theory, the static nonlinear Hall current is [4, 41–44]

$$\vec{\mathcal{J}}_H = -\frac{\tau}{2} \hat{z} \times \mathcal{E} (\mathbf{D} \cdot \mathcal{E}), \quad (4)$$

with  $\tau$  the relaxation time and  $\mathbf{D}$  the dipolar component vector in two dimensions. When a single mirror plane  $\mathcal{M}_x$  is preserved, symmetry enforces  $\mathcal{D}^{yz} = 0$  while allowing  $\mathcal{D}^{xz} \neq 0$  [45]. For an in-plane electric field  $\mathcal{E} = \mathcal{E}(\cos \theta, \sin \theta)$ , the nonlinear Hall response therefore obeys  $\mathcal{J}_H = \sigma_H(\theta) |\mathcal{E}|^2$  with  $\sigma_H(\theta) = -(\tau/2) \mathcal{D}^{xz} \sin \theta$ .

The energy-resolved response in Fig. 2(b) shows that the dominant contribution to  $\mathcal{D}^{xz}$  comes from the SOC-split Dirac crossings identified in Fig. 2(a). In the onsite-modulated model, uniaxial 2% strain together with SOC yields a peak value  $D^{xz} \sim 0.2 \text{ \AA}$  near  $\lambda_{\text{SO}} = 0.056t$ . In the breathing case, the corresponding peak is  $D^{xz} \sim 0.05 \text{ \AA}$  near  $\lambda_{\text{SO}} = 0.04t$  [Supplementary Fig. S3.1]. Taking  $\tau = 10 \text{ ps}$ , these values translate into nonlinear Hall conductivities of order  $\sigma_H \sim 0.037 \text{ nm S V}^{-1}$

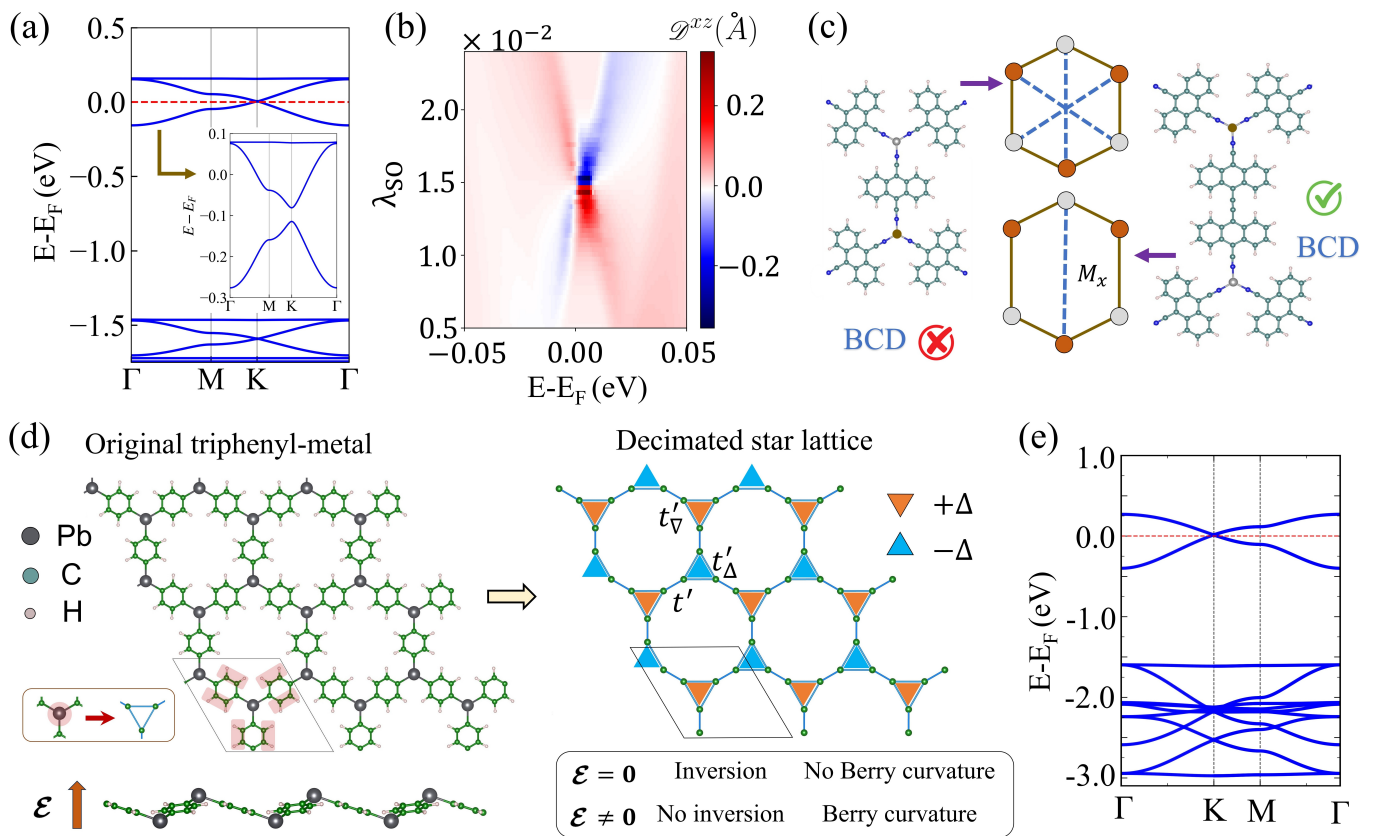


FIG. 3. **Dipolar component of Berry curvature in metal-organic frameworks.** (a) DFT band structure of Cu-DCA showing two energetically separated kagome-like band manifolds, with the Fermi level located close to the Dirac point of the upper kagome-like band. Inset: replacing one Cu atom by Zn provides one route to inversion-symmetry breaking. (b) Phase diagram for the dipolar component obtained from DFT-consistent hopping parameters ( $t_{\Delta} = t_{\nabla} = -0.11$  eV,  $t = 0.81$  eV, and  $t_{\perp} = -0.78$  eV) in the presence of SOC, inversion-symmetry breaking, and 2% uniaxial strain. The dipolar component switches sign across the topological transition. (c) Proposed synthesis-based route for generating the required symmetry lowering intrinsically, by modifying one of the three equivalent linker directions. (d) Generalization to a triphenyl-metal MOF (Pb shown here), which can likewise be downfolded to a star lattice. Because the two Pb sites lie on different planes, a transverse electric field can break inversion symmetry. (e) DFT band structure of the pristine triphenyl-Pb framework, showing the characteristic star-lattice-like band structure.

and  $\sigma_H \sim 0.01$  nmSV<sup>-1</sup>, respectively; see Supplementary Sec. S4. The sharp enhancement and sign reversal of the dipolar component across the transition are thus direct consequences of SOC-driven band inversion in the effective star lattice.

*Material implementation and design principles.* — Having identified the band-geometry mechanism in the effective model, we now return to the material level. Figure 3(a) shows that the DFT band structure of Cu-DCA indeed contains two energetically separated kagome-like band manifolds, with the Fermi level lying close to the Dirac point of the upper one. Using the DFT-consistent hoppings  $t_{\Delta} = t_{\nabla} = -0.11$  eV,  $t = 0.81$  eV, and  $t_{\perp} = -0.78$  eV, we compute the dipolar component phase diagram shown in Fig. 3(b). The response is maximized near the topological phase boundary, where the SOC-induced avoided crossing produces strongly concentrated Berry curvature and a sign change of the dipolar com-

ponent. This demonstrates that the effective star-lattice description captures not only the band structure but also the symmetry-controlled nonlinear response of the MOF.

In Cu-DCA, inversion symmetry can be broken by an appropriate substrate, by heterostructure engineering, or by chemical substitution, as illustrated by the Zn-doped configuration in the inset of Fig. 3(a). In addition, the uniaxial anisotropy required to expose a nonzero  $\mathcal{D}^{xz}$  need not be supplied externally. Figure 3(c) sketches a synthesis-based route in which one of the three equivalent linker directions is modified, for example by directly connecting two anthracene-like units or by inserting an acetylenic bridge [46, 47]. In the decimated description, this changes the effective hopping between the terminal sites  $L$  and  $R$  of Fig. 1(c) from  $t = -\lambda'^2/\lambda$  to an anisotropic value  $t_{\perp} = (t_3/\lambda)t$  along the selected direction, where  $t_3$  is the hopping amplitude through the modified bridge. The resulting structure lowers the orig-

inal  $C_3$  symmetry to a single mirror plane and simultaneously removes inversion, thereby generating the finite Berry curvature and the symmetry-allowed dipolar component needed for the NLHE without externally applied strain.

Using Eq. (4), we estimate the experimentally observable response for two symmetry-lowered realizations: on-site modulation and breathing-type intra-triangle hopping modulation. For an in-plane electric field of magnitude  $\mathcal{E} \sim 10^4$  V/m, the expected nonlinear Hall current reaches  $\mathcal{J}_H \sim 0.037$  mA/cm in the onsite-modulated case and  $\mathcal{J}_H \sim 0.01$  mA/cm in the breathing case (Supplementary Sec. S4). These values fall within current experimental sensitivity.

The design principle is not restricted to Cu–DCA. As illustrated in Fig. 3(d), a second class of  $C_3$ -symmetric MOFs—exemplified by a triphenyl–Pb framework—can likewise be downfolded to an effective star-lattice description, with a hopping amplitude of  $t' = -2t$  between neighboring triangles. In this case, the two Pb sites in the unit cell lie on different planes, producing an intrinsically buckled structure. A transverse electric field, for instance, from an underlying substrate, can lift the remaining inversion symmetry in a controlled manner. When combined with SOC, this controlled inversion symmetry breaking provides the essential ingredients for generating finite Berry curvature and its associated dipolar response. The pristine DFT band structure in Fig. 3(e) closely follows the characteristic star-lattice dispersion, validating the downfolded description. The same symmetry mechanism identified for Cu–DCA—namely, selectively extending one-third of the linkages between nearest-neighbor triangles through direct benzene-ring coupling or via acetylene bridges—should likewise generate a finite NLHE in this broader class of MOFs. More generally, any  $C_3$ -symmetric MOF in which a metal center connects three symmetry-related nonmetal sites provides a natural starting point for an effective star-lattice description and, consequently, for tunable NLHE physics. Related MOF platforms such as  $\text{Ni}_2\text{C}_{24}\text{S}_6\text{H}_{12}$  [48] and suitably designed covalent organic frameworks [49, 50] or conjugated polymer networks [51] appear promising in

the same spirit.

*Conclusions.*— We have established a concrete design principle for realizing nonlinear Hall physics in metal-organic frameworks by combining analytical downfolding, symmetry analysis, and first-principles calculations. For the experimentally relevant Cu–DCA monolayer, the real-space decimation procedure yields an effective star-lattice model whose renormalized parameters reproduce the essential low-energy electronic structure, including the separated kagome-like bands and the Dirac feature near the Fermi level. Within this effective description, we showed that inversion-symmetry breaking together with intrinsic spin-orbit coupling produces strong Berry-curvature hot spots and a tunable Berry-curvature dipole, with a characteristic enhancement and sign reversal across the topological transition. These results provide a direct route to engineer an observable nonlinear Hall response in Cu–DCA through substrate effects, doping, strain, or, more appealingly, through symmetry-selective chemical synthesis that embeds the required anisotropy into the framework itself. Beyond Cu–DCA, our analysis identifies a broader class of  $C_3$ -symmetric MOFs, including triphenyl–metal networks, that can be mapped to the same effective star-lattice geometry and are therefore natural candidates for analogous nonlinear transport responses. Overall, this work positions two-dimensional MOFs as a highly tunable materials platform for exploring Berry-phase-driven transport, topological band engineering, and nonlinear quantum phenomena.

*Acknowledgments.*— The authors gratefully acknowledge the Gauss Centre for Supercomputing e.V. (www.gauss-centre.eu) for funding this project by providing computing time on the GCS Supercomputer SuperMUC-NG at Leibniz Supercomputing Centre (www.lrz.de). The authors also acknowledge financial support by the Deutsche Forschungsgemeinschaft through Project-ID 258499086 – SFB 1170, through the Würzburg–Dresden Cluster of Excellence on Complexity and Topology in Quantum Matter – ctd.qmat, Project-ID 390858490 – EXC 2147, and through the Research Unit QUASt, Project-ID 449872909 – FOR5249. A.N. acknowledges support from DST CRG grant (CRG/2023/000114).

## I. SUPPLEMENTARY MATERIAL

This Supplementary Material provides additional details supporting the main text of “Nonlinear Hall Effect in Metal–Organic Frameworks”.

### SUPPLEMENTARY CONTENTS

I. Supplementary Material	5
Supplementary Contents	5
S1. Effective star-lattice model	6

A. Hamiltonian

6

B. Representative band structures

6

S2. Wannier charge centers and the  $\mathbb{Z}_2$  invariant

6

S3. Berry-curvature response in the breathing star lattice

7

S4. Nonlinear Hall conductivity estimates

7

S5. Methodology

8

A. DFT methodology

8

B. Real-space decimation

8

## S1. EFFECTIVE STAR-LATTICE MODEL

### A. Hamiltonian

The effective star-lattice Hamiltonian is written as

$$\mathcal{H} = \mathcal{H}_0 + \mathcal{H}_\delta + \mathcal{H}_{\text{SO}}. \quad (\text{S1.1})$$

The spin-independent hopping part reads

$$\begin{aligned} \mathcal{H}_0 = & -t_\Delta \sum_{\langle ij \rangle \in \Delta} c_{i\sigma}^\dagger c_{j\sigma} - t_\nabla \sum_{\langle ij \rangle \in \nabla} c_{i\sigma}^\dagger c_{j\sigma} \\ & - t \sum_{\langle ij \rangle \in \sigma} c_{i\sigma}^\dagger c_{j\sigma} + \text{h.c.}, \end{aligned} \quad (\text{S1.2})$$

where  $t_\Delta$  and  $t_\nabla$  are the intra-triangle hoppings on the two inequivalent triangular motifs of the star lattice, while  $t$  denotes the inter-triangle hopping in the pristine system. A breathing distortion corresponds to  $t_\Delta \neq t_\nabla$ , and uniaxial anisotropy is modeled by replacing one of the inter-triangle hoppings by  $t_\perp$ .

Inversion-symmetry breaking through onsite modulation is captured by

$$\mathcal{H}_\delta = \delta_1 \sum_{i \in \Delta} c_{i\sigma}^\dagger c_{i\sigma} + \delta_2 \sum_{i \in \nabla} c_{i\sigma}^\dagger c_{i\sigma}, \quad (\text{S1.3})$$

where  $\delta_1$  and  $\delta_2$  are onsite energies on the two triangular subunits.

The intrinsic spin-orbit coupling is taken in Kane-Mele form,

$$\mathcal{H}_{\text{SO}} = i\lambda_{\text{SO}} \sum_{\langle\langle ij \rangle\rangle, \alpha, \beta} \nu_{ij} c_{i\alpha}^\dagger (s^z)_{\alpha\beta} c_{j\beta} + \text{h.c.}, \quad (\text{S1.4})$$

where  $\lambda_{\text{SO}}$  is the SOC strength,  $\nu_{ij} = \pm 1$  encodes the chirality of the hopping path, and  $(s^z)_{\alpha\beta}$  is the spin matrix.

### B. Representative band structures

Figure S1.1 shows representative band structures of the pristine star lattice along the high-symmetry path

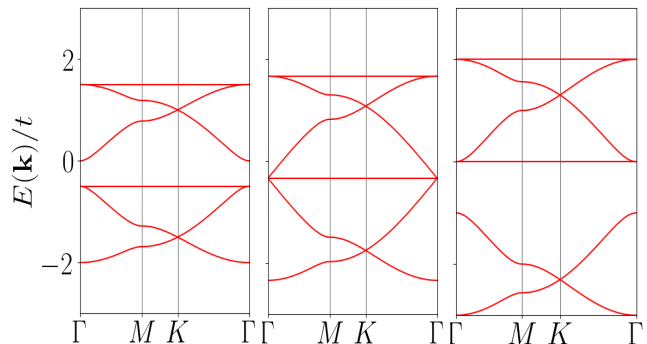


FIG. S1.1. **Representative band structures of the pristine star lattice.** Band structures along  $\Gamma \rightarrow M \rightarrow K \rightarrow \Gamma$  for  $t_\Delta = t_\nabla = 0.5t$ ,  $t_\Delta = t_\nabla = \frac{2}{3}t$ , and  $t_\Delta = t_\nabla = t$ . Throughout the calculations, we set  $t = 1$  eV.

$\Gamma \rightarrow M \rightarrow K \rightarrow \Gamma$ . By tuning the ratio between intra-triangle and inter-triangle hoppings, the model interpolates between dispersions with different degrees of kagome-like character. The regime emphasized in the main text is the one with two well-separated kagome-like band manifolds, because this reproduces the DFT band structure of Cu-DCA most closely and places the Fermi level near Dirac crossings that can be converted into Berry-curvature hot spots once SOC and inversion-symmetry breaking are introduced.

## S2. WANNIER CHARGE CENTERS AND THE $\mathbb{Z}_2$ INVARIANT

The maximally localized Wannier function associated with band index  $n$  in the unit cell located at Bravais lattice vector  $\mathbf{R}$  is defined as the Fourier transform of the Bloch states,

$$|\mathbf{R}n\rangle = \frac{V_{\text{uc}}}{(2\pi)^d} \int_{\text{BZ}} d^d\mathbf{k} e^{i\mathbf{k}\cdot\mathbf{R}} |\psi_{n\mathbf{k}}\rangle, \quad (\text{S2.1})$$

where  $d$  is the spatial dimension,  $V_{\text{uc}}$  is the  $d$ -dimensional unit-cell volume (area in two dimensions), and  $|\psi_{n\mathbf{k}}\rangle = e^{i\mathbf{k}\cdot\hat{\mathbf{r}}} |u_{n\mathbf{k}}\rangle$  with  $|u_{n\mathbf{k}}\rangle$  the lattice-periodic Bloch function. The Wannier charge center (WCC) along  $\hat{x}$  for the home cell ( $\mathbf{R} = 0$ ) is

$$\bar{x}_n = \langle \mathbf{0}n | \hat{x} | \mathbf{0}n \rangle. \quad (\text{S2.2})$$

In time-reversal-invariant systems, the occupied subspace can be organized into Kramers pairs labeled by  $S = I, II$ . For a given branch  $S$ , the Berry connection is

$$\mathbf{A}^S(\mathbf{k}) = i \sum_{\alpha} \langle u_{\alpha\mathbf{k}}^S | \nabla_{\mathbf{k}} | u_{\alpha\mathbf{k}}^S \rangle, \quad (\text{S2.3})$$

and the corresponding WCC can be written as the Brillouin-zone average

$$\bar{x}_n^S = \frac{V_{\text{uc}}}{(2\pi)^d} \int_{\text{BZ}} d^d\mathbf{k} \langle u_{n\mathbf{k}}^S | i \frac{\partial}{\partial k_x} | u_{n\mathbf{k}}^S \rangle. \quad (\text{S2.4})$$

To diagnose the topological phase transition discussed in the main text, we track the WCC flow as a function of  $k_y$  for two representative symmetry-lowered star-lattice realizations. Figure S2.1(a,b) shows the onsite-modulated model with  $\delta_1 = -0.08t$ ,  $\delta_2 = 0.08t$ , and  $t_{\Delta} = t_{\nabla} = 0.5t$  for two values of  $\lambda_{\text{SO}}$ . As the SOC strength is increased from  $0.04t$  to  $0.06t$ , the WCC flow changes from a topologically trivial to a nontrivial pattern, consistent with the band inversion at the  $K$  point. Figure S2.1(c,d) shows the same analysis for the breathing star lattice with  $t_{\Delta} = 0.45t$  and  $t_{\nabla} = 0.5t$ , where the transition occurs between  $\lambda_{\text{SO}} = 0.03t$  and  $0.04t$ .

The  $\mathbb{Z}_2$  invariant is obtained by counting the number of WCC crossings with a reference line over half of the Brillouin zone [52, 53]. An odd number of crossings signals a topologically nontrivial phase, whereas an even number indicates a trivial phase.

### S3. BERRY-CURVATURE RESPONSE IN THE BREATHING STAR LATTICE

In the main text, the onsite-modulated star lattice was used to illustrate the emergence of Berry-curvature hot spots and of a large BCD near the topological transition. The breathing star lattice shows the same qualitative physics and provides an independent route to inversion-symmetry breaking.

Figure S3.1(a) displays the Berry-curvature-projected band structure of the breathing model with  $t_{\Delta} = 0.45t$  and  $t_{\nabla} = 0.5t$  for two representative values of  $\lambda_{\text{SO}}$ . Increasing  $\lambda_{\text{SO}}$  from  $0.03t$  to  $0.04t$  induces a band inversion near the  $K$  point in the positive-energy sector. Correspondingly, the Berry-curvature hot spots at the avoided crossings reverse sign, reflecting the change in band character across the inversion.

The resulting BCD is shown in Fig. S3.1(b) for the same breathing model in the presence of a small inter-triangle anisotropy  $t_{\perp} \neq t$ , taken to represent a 2% tensile strain. As in the onsite-modulated case, the dominant contribution is concentrated near the SOC-split Dirac crossings. The BCD therefore exhibits a pronounced enhancement close to the critical SOC strength and changes sign across the topological transition.

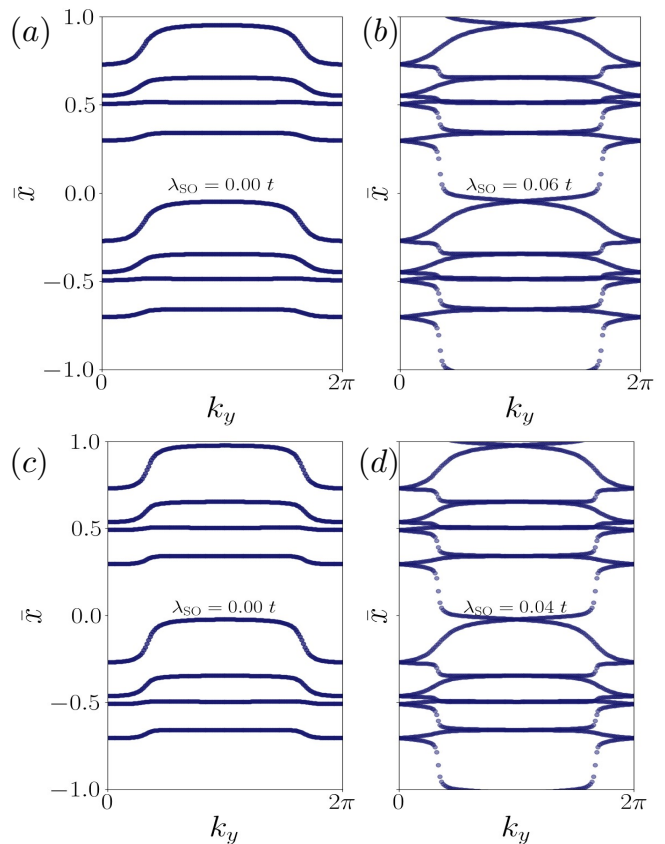


FIG. S2.1. **Wannier charge centers and topological phase transition.** Upper panels (a,b): WCC evolution for the onsite-modulated model with  $\delta_1 = -0.08t$ ,  $\delta_2 = 0.08t$ , and  $t_{\Delta} = t_{\nabla} = 0.5t$ . Lower panels (c,d): WCC evolution for the breathing star lattice with  $t_{\Delta} = 0.45t$  and  $t_{\nabla} = 0.5t$ . In both cases, increasing  $\lambda_{\text{SO}}$  drives a  $\mathbb{Z}_2$  transition. An odd (even) number of crossings of a reference line within half of the Brillouin zone identifies the nontrivial (trivial) phase.

### S4. NONLINEAR HALL CONDUCTIVITY ESTIMATES

To estimate the experimentally relevant NLHE response, we evaluate the angular dependence of the nonlinear Hall conductivity using Eq. (4) of the main text. Figure S4.1 shows the result for two symmetry-lowered realizations of the star lattice: onsite modulation and breathing-type intra-triangle hopping modulation. In both cases, the response follows the mirror-constrained angular dependence expected for a system with a single remaining mirror plane  $\mathcal{M}_x$ .

For an in-plane electric field of magnitude  $\mathcal{E} \sim 10^4$  V/m applied at an angle  $\theta$  relative to  $\mathcal{M}_x$ , the nonlinear Hall current takes the form  $(\mathcal{J}_x, \mathcal{J}_y) = \mathcal{J}_H(\cos\theta, -\sin\theta)$  [44]. Using the BCD values discussed in the main text and a representative relaxation time  $\tau = 10$  ps, we obtain  $\mathcal{J}_H \sim 0.037$  mA/cm for the onsite-modulated case and  $\mathcal{J}_H \sim 0.01$  mA/cm for the breathing case. These values are within the reach of present exper-

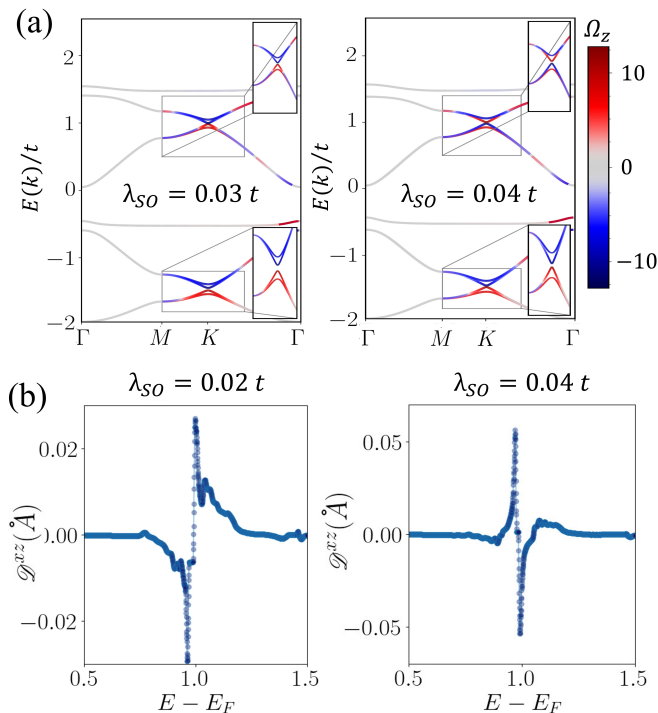


FIG. S3.1. **Berry curvature and Berry-curvature dipole in the breathing star lattice.** (a) Berry-curvature-projected band structure for the breathing model with  $t_{\Delta} = 0.45t$  and  $t_{\nabla} = 0.5t$ , shown for two SOC strengths. (b) Corresponding BCD in the presence of a small anisotropy  $t_{\perp} \neq t$  representing 2% tensile strain. The peak enhancement and sign reversal track the topological transition.

imental sensitivity.

## S5. METHODOLOGY

### A. DFT methodology

First-principles calculations were performed within density functional theory using the QUANTUM ESPRESSO package [54, 55]. Exchange-correlation effects were treated within the Perdew–Burke–Ernzerhof generalized-gradient approximation [56], using the projector-augmented-wave framework [57]. Scalar-relativistic and fully relativistic pseudopotentials were employed for calculations without and with SOC, respectively. We used a kinetic-energy cutoff of 46 Ry and an  $8 \times 8 \times 1$  Monkhorst–Pack  $k$  mesh [58]. A vacuum spacing of 10 Å was introduced along the out-of-plane direction to suppress interlayer interactions. Topological properties and Berry-curvature-related observables were additionally benchmarked using the WannierBerri package [59], interfaced with PythTB [60].

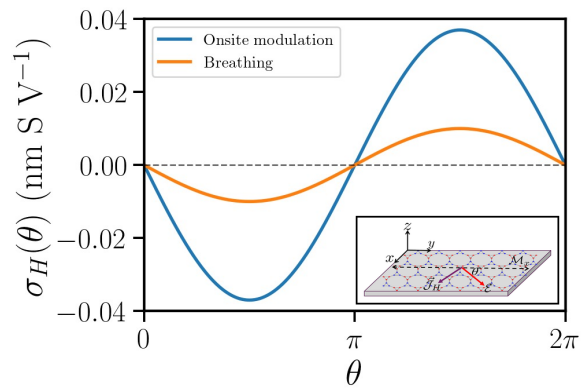


FIG. S4.1. **Angular dependence of the nonlinear Hall conductivity.** Angular dependence of  $\sigma_H(\theta)$  for the onsite-modulated and breathing realizations. Inset: geometry of the in-plane electric field  $\mathcal{E}$  (red arrow) applied at an angle  $\theta$  relative to the mirror axis  $\mathcal{M}_x$ , generating a transverse nonlinear Hall current  $\mathcal{J}_H$  (blue arrow).

### B. Real-space decimation

The tight-binding form of the Schrödinger equation is

$$(E - \varepsilon_i)\phi_i = \sum_j t_{ij}\phi_j, \quad (\text{S5.1})$$

where  $E$  is the eigenenergy,  $\varepsilon_i$  is the onsite potential on site  $i$ ,  $\phi_i$  is the corresponding wave-function amplitude, and  $t_{ij}$  is the hopping amplitude between sites  $i$  and  $j$ .

For the linker segment connecting neighboring effective triangles [Fig. 1(c) of the main text], the local difference equations for the site pair  $(i, j)$  can be written as

$$(E - \varepsilon)\phi_{i/j} = \lambda\phi_{j/i} + \lambda\phi_{g/h}, \quad (\text{S5.2})$$

where  $\lambda$  denotes the nearest-neighbor hopping within the linker. Substituting Eq. (S5.2) into the corresponding equation for the next pair  $(g, h)$ ,

$$(E - \varepsilon)\phi_{g/h} = \lambda\phi_{i/j} + \lambda\phi_{e/f}, \quad (\text{S5.3})$$

and taking the low-energy condition  $E - \varepsilon \approx 0$ , one obtains

$$(E - \varepsilon)\phi_{g/h} = -\lambda\phi_{h/g} + \lambda\phi_{e/f}. \quad (\text{S5.4})$$

This identifies the first renormalized hopping as  $u = -\lambda$ .

Iterating the same decimation step through the sequence of pairs  $\{(g, h), (e, f), (c, d), (a, b)\}$  reduces the full linker segment to an effective bond between the terminal sites  $L$  and  $R$  shown in Fig. 1(c) of the main text. The resulting renormalized parameters are

$$v = 2\lambda, \quad w = -\lambda, \quad x = \lambda, \quad t = -\frac{\lambda'^2}{\lambda}. \quad (\text{S5.5})$$

This analytical decimation establishes the effective star-lattice description used throughout the main text and provides the basis for relating the chemistry of the MOF linkers to the symmetry-selective hopping amplitudes of the low-energy model.

- [1] K. v. Klitzing, G. Dorda, and M. Pepper, New method for high-accuracy determination of the fine-structure constant based on quantized hall resistance, *Phys. Rev. Lett.* **45**, 494 (1980).
- [2] D. Xiao, M.-C. Chang, and Q. Niu, Berry phase effects on electronic properties, *Rev. Mod. Phys.* **82**, 1959 (2010).
- [3] N. Nagaosa, J. Sinova, S. Onoda, A. H. MacDonald, and N. P. Ong, Anomalous hall effect, *Rev. Mod. Phys.* **82**, 1539 (2010).
- [4] I. Sodemann and L. Fu, Quantum nonlinear hall effect induced by berry curvature dipole in time-reversal invariant materials, *Phys. Rev. Lett.* **115**, 216806 (2015).
- [5] Z. Du, H.-Z. Lu, and X. Xie, Nonlinear hall effects, *Nature Reviews Physics* **3**, 744 (2021).
- [6] C. Ortix, Nonlinear hall effect with time-reversal symmetry: Theory and material realizations, *Advanced Quantum Technologies* **4**, 2100056 (2021).
- [7] A. Bandyopadhyay, N. B. Joseph, and A. Narayan, Nonlinear hall effects: Mechanisms and materials, *Materials Today Electronics* **8**, 100101 (2024).
- [8] Q. Ma, S.-Y. Xu, H. Shen, D. MacNeill, V. Fatemi, T.-R. Chang, A. M. Mier Valdivia, S. Wu, Z. Du, C.-H. Hsu, *et al.*, Observation of the nonlinear hall effect under time-reversal-symmetric conditions, *Nature* **565**, 337 (2019).
- [9] K. Kang, T. Li, E. Sohn, J. Shan, and K. F. Mak, Nonlinear anomalous hall effect in few-layer wte<sub>2</sub>, *Nature materials* **18**, 324 (2019).
- [10] P. Makushko, S. Kovalev, Y. Zabala, I. Ilyakov, A. Ponomaryov, A. Arshad, G. L. Prajapati, T. V. A. G. de Oliveira, J.-C. Deinert, P. Chekhonin, I. Veremchuk, T. Kosub, Y. Skourski, F. Ganss, D. Makarov, and C. Ortix, A tunable room-temperature nonlinear hall effect in elemental bismuth thin films, *Nature Electronics* **7**, 207 (2024).
- [11] L. Min, H. Tan, Z. Xie, L. Miao, R. Zhang, S. H. Lee, V. Gopalan, C.-X. Liu, N. Alem, B. Yan, and Z. Mao, Strong room-temperature bulk nonlinear hall effect in a spin-valley locked dirac material, *Nature Communications* **14**, 364 (2023).
- [12] S. Sinha, P. C. Adak, A. Chakraborty, K. Das, K. Deb Nath, L. D. V. Sangani, K. Watanabe, T. Taniguchi, U. V. Waghmare, A. Agarwal, and M. M. Deshmukh, Berry curvature dipole senses topological transition in a moiré superlattice, *Nature Physics* **18**, 765 (2022).
- [13] X.-G. Ye, H. Liu, P.-F. Zhu, W.-Z. Xu, S. A. Yang, N. Shang, K. Liu, and Z.-M. Liao, Control over berry curvature dipole with electric field in wte<sub>2</sub>, *Physical Review Letters* **130**, 016301 (2023).
- [14] T. Nomoto, A. Kikkawa, K. Nakazawa, *et al.*, Observation of the nonlinear chiral thermoelectric hall effect in tellurium, *Nature Physics* (2025).
- [15] D. Kumar, C.-H. Hsu, R. Sharma, T.-R. Chang, P. Yu, J. Wang, G. Eda, G. Liang, and H. Yang, Room-temperature nonlinear hall effect and wireless radiofrequency rectification in weyl semimetal TaIrTe<sub>4</sub>, *Nature Nanotechnology* **16**, 421 (2021).
- [16] H. Wang and X. Qian, Ferroicity-driven nonlinear photocurrent switching in time-reversal invariant ferroic materials, *Science Advances* **5**, eaav9743 (2019).
- [17] J. Kim, K.-W. Kim, D. Shin, S.-H. Lee, J. Sinova, N. Park, and H. Jin, Prediction of ferroelectricity-driven Berry curvature enabling charge- and spin-controllable photocurrent in tin telluride monolayers, *Nature Communications* **10**, 3965 (2019).
- [18] T. Rangel, B. M. Fregoso, B. S. Mendoza, T. Morimoto, J. E. Moore, and J. B. Neaton, Large bulk photovoltaic effect and spontaneous polarization of single-layer monochalcogenides, *Phys. Rev. Lett.* **119**, 067402 (2017).
- [19] H.-C. Zhou, J. R. Long, and O. M. Yaghi, Introduction to metal-organic frameworks, *Chemical Reviews* **112**, 673 (2012).
- [20] H. Furukawa, K. E. Cordova, M. O’Keeffe, and O. M. Yaghi, The chemistry and applications of metal-organic frameworks, *Science* **341**, 1230444 (2013).
- [21] W. Jiang, X. Ni, and F. Liu, Exotic topological bands and quantum states in metal-organic and covalent-organic frameworks, *Accounts of Chemical Research* **54**, 416 (2021).
- [22] Z. Wang, Z. Liu, and F. Liu, Organic topological insulators in organometallic lattices, *Nature Communications* **4**, 1471 (2013).
- [23] Z. F. Wang, Z. Liu, and F. Liu, Quantum anomalous hall effect in 2d organic topological insulators, *Phys. Rev. Lett.* **110**, 196801 (2013).
- [24] Z. Wang, N. Su, and F. Liu, Prediction of a two-dimensional organic topological insulator, *Nano Letters* **13**, 2842 (2013).
- [25] T. Hu, W. Zhong, T. Zhang, W. Wang, Z. F. Wang, *et al.*, Identifying topological corner states in two-dimensional metal-organic frameworks, *Nature Communications* **14**, 7092 (2023).
- [26] P. Tin, M. J. Jenkins, J. Xing, N. Caci, Z. Gai, R. Jin, S. Wessel, J. Krzystek, C. Li, L. L. Daemen, Y. Cheng, and Z.-L. Xue, Haldane topological spin-1 chains in a planar metal-organic framework, *Nature Communications* **14**, 5454 (2023).
- [27] M. Fuchs, P. Liu, T. Schwemmer, G. Sangiovanni, R. Thomale, C. Franchini, and D. Di Sante, Kagome metal-organic frameworks as a platform for strongly correlated electrons, *Journal of Physics: Materials* **3**, 025001 (2020).
- [28] L. Z. Zhang, Z. F. Wang, B. Huang, B. Cui, Z. Wang, S. X. Du, H.-J. Gao, and F. Liu, Intrinsic two-dimensional organic topological insulators in metal-dicyanoanthracene lattices, *Nano Letters* **16**, 2072 (2016).
- [29] A. Kumar, K. Banerjee, A. S. Foster, and P. Liljeroth, Two-dimensional band structure in honeycomb metal-organic frameworks, *Nano Letters* **18**, 5596 (2018).
- [30] Z. Wang, Z. Liu, and F. Liu, Quantum anomalous hall effect in 2d organic topological insulators, *Physical Review Letters* **110**, 196801 (2013).
- [31] A. Bandyopadhyay, A. Majumdar, S. Chowdhury, R. Ahuja, and D. Jana, 8-16-4 graphyne: Square-lattice two-dimensional nodal line semimetal with a nontrivial topological Zak index, *Physical Review B* **103**, 075137 (2021).
- [32] A. Bandyopadhyay and D. Jana, A review on role of tetra-rings in graphene systems and their possible applications, *Reports on Progress in Physics* **83**, 056501 (2020).
- [33] A. Banerjee, A. Bandyopadhyay, R. Sarkar, and

- A. Narayan, Non-hermitian topology and flat bands via an exact real-space decimation scheme, *Physical Review B* **110**, 085431 (2024).
- [34] A. Bose, A. Bandyopadhyay, and A. Narayan, Origin of flat bands and non-trivial topology in coupled kagome lattices, *Communications Physics* **8**, 519 (2025).
- [35] D. Kumar, J. Hellerstedt, B. Field, B. Lowe, Y. Yin, N. V. Medhekar, and A. Schiffrin, Manifestation of strongly correlated electrons in a 2d kagome metal-organic framework, *Advanced Functional Materials* **31**, 2106474 (2021).
- [36] J. Zhang, A. Shchyrba, S. Nowakowska, E. Meyer, T. A. Jung, and M. Muntwiler, Probing the spatial and momentum distribution of confined surface states in a metal coordination network, *Chemical Communications* **50**, 12289 (2014).
- [37] L. Hernández-López, I. Piquero-Zulaica, C. A. Downing, M. Piantek, J. Fujii, D. Serrate, J. E. Ortega, F. Bartolomé, and J. Lobo-Checa, Searching for kagome multi-bands and edge states in a predicted organic topological insulator, *Nanoscale* **13**, 5216 (2021).
- [38] L. Yan, O. J. Silveira, B. Alldritt, S. Kezilebieke, A. S. Foster, and P. Liljeroth, Two-dimensional metal-organic framework on superconducting nbse<sub>2</sub>, *ACS Nano* **15**, 17813 (2021).
- [39] L. Yan, O. J. Silveira, B. Alldritt, O. Krejčí, A. S. Foster, and P. Liljeroth, Synthesis and local probe gating of a monolayer metal-organic framework, *Advanced Functional Materials* **31**, 2100519 (2021).
- [40] L. Z. Zhang, Z. F. Wang, B. Huang, B. Cui, Z. Wang, S. X. Du, H.-J. Gao, and F. Liu, Intrinsic two-dimensional organic topological insulators in metal-dicyanoanthracene lattices, *Nano Letters* **16**, 2072 (2016).
- [41] J.-S. You, S. Fang, S.-Y. Xu, E. Kaxiras, and T. Low, Berry curvature dipole current in the transition metal dichalcogenides family, *Phys. Rev. B* **98**, 121109 (2018).
- [42] R. Battilomo, N. Scopigno, and C. Ortix, Berry curvature dipole in strained graphene: A fermi surface warping effect, *Phys. Rev. Lett.* **123**, 196403 (2019).
- [43] T. Low, Y. Jiang, and F. Guinea, Topological currents in black phosphorus with broken inversion symmetry, *Phys. Rev. B* **92**, 235447 (2015).
- [44] Y. Zhao, J. Cao, Z. Zhang, S. Li, Y. Li, F. Ma, and S. A. Yang, Berry curvature dipole and nonlinear hall effect in two-dimensional nb<sub>2n+1</sub>si<sub>n</sub>te<sub>4n+2</sub>, *Phys. Rev. B* **107**, 205124 (2023).
- [45] A. Bandyopadhyay, N. B. Joseph, and A. Narayan, Electrically switchable giant berry curvature dipole in silicene, germanene and stanene, *2D Materials* **9**, 035013 (2022).
- [46] B. Cirera, A. Sánchez-Grande, B. De la Torre, J. Santos, S. Edalatmanesh, E. Rodríguez-Sánchez, K. Lauwaet, B. Mallada, R. Zbořil, R. Miranda, *et al.*, Tailoring topological order and  $\pi$ -conjugation to engineer quasi-metallic polymers, *Nature nanotechnology* **15**, 437 (2020).
- [47] S. Kawai, O. Krejci, A. S. Foster, R. Pawlak, F. Xu, L. Peng, A. Orita, and E. Meyer, Diacetylene linked anthracene oligomers synthesized by one-shot homocoupling of trimethylsilyl on cu(111), *ACS Nano* **12**, 8791 (2018).
- [48] L. Wei, X. Zhang, and M. Zhao, Spin-polarized dirac cones and topological nontriviality in a metal-organic framework ni<sub>2</sub>c<sub>24</sub>s<sub>6</sub>h<sub>12</sub>, *Physical Chemistry Chemical Physics* **18**, 8059 (2016).
- [49] Y. Yan, F. Liu, W. Tang, H. X. Wong, B. Qie, S. G. Louie, and F. R. Fischer, Engineering phase-frustration-induced flat bands in an aza-triangulene covalent kagome lattice, *Nature Materials* **1** (2026).
- [50] L. Yang, J. Dong, Z. Wang, D. Li, C. Chen, B. Huang, D. Liu, and B. Cui, Breathing-controlled pure orbital and nonlinear hall effects in 2d organic kagome frameworks, *Nano Letters* **26**, 1455 (2026).
- [51] J.-J. Adjizian, P. Briddon, B. Humbert, J.-L. Duvail, P. Wagner, C. Adda, and C. Ewels, Dirac cones in two-dimensional conjugated polymer networks, *Nature Communications* **5**, 5842 (2014).
- [52] A. A. Soluyanov and D. Vanderbilt, Computing topological invariants without inversion symmetry, *Phys. Rev. B* **83**, 235401 (2011).
- [53] R. Yu, X. L. Qi, A. Bernevig, Z. Fang, and X. Dai, Equivalent expression of z<sub>2</sub> topological invariant for band insulators using the non-abelian berry connection, *Phys. Rev. B* **84**, 075119 (2011).
- [54] P. Giannozzi, S. Baroni, N. Bonini, M. Calandra, R. Car, C. Cavazzoni, D. Ceresoli, G. L. Chiarotti, M. Cococcioni, I. Dabo, *et al.*, Quantum espresso: a modular and open-source software project for quantum simulations of materials, *Journal of Physics: Condensed Matter* **21**, 395502 (2009).
- [55] P. Giannozzi, O. Andreussi, T. Brumme, O. Bunau, M. B. Nardelli, M. Calandra, R. Car, C. Cavazzoni, D. Ceresoli, M. Cococcioni, I. Dabo, A. Dal Corso, S. de Gironcoli, *et al.*, Advanced capabilities for materials modelling with Quantum ESPRESSO, *Journal of Physics: Condensed Matter* **29**, 465901 (2017).
- [56] J. P. Perdew, K. Burke, and M. Ernzerhof, Generalized gradient approximation made simple, *Physical Review Letters* **77**, 3865 (1996).
- [57] P. E. Blöchl, Projector augmented-wave method, *Physical Review B* **50**, 17953 (1994).
- [58] H. J. Monkhorst and J. D. Pack, Special points for brillouin-zone integrations, *Physical Review B* **13**, 5188 (1976).
- [59] S. S. Tsirkin, High performance wannier interpolation of berry curvature and related quantities with wannierberri code, *npj Computational Materials* **7**, 33 (2021).
- [60] S. Coh and D. Vanderbilt, *Python tight binding (pythtb)* (2022).